

Detection and Imaging of Moving Targets with LiMIT SAR Data

Michael Newey, Gerald Benitz, David Barrett

MIT Lincoln Laboratory

Lexington, Massachusetts 02420 USA

Email: michael.newey@ll.mit.edu

Telephone: (781) 981-0347

Fax: (781) 981-5234

Sandeep Mishra BAE Systems Inc

Nashua, NH 03060 USA

Email: sandeep.mishra@baesystems.com

Distribution A: Public Release

Abstract

Detecting moving targets in SAR imagery has recently gained a lot of interest as a way to replace optical moving target detection and classification in adverse (e.g. cloudy) weather conditions. This can be particularly important for small radar antennas, which tend to have high conventional GMTI minimum detectable velocity. In this work, we primarily focus on the problem of detecting and imaging the targets in single channel (or summed multi-channel) SAR data. Single channel based methods provide the ability to do detection well below the normal minimum detectable velocity of multi-channel based GMTI. We also show results for multiple channel geo-location after single-channel detection and imaging.

The algorithms consist of the following steps: We first suppress the stationary scene by comparing non-coherent time-subimages. We then detect the movers by applying a set of possible motion corrections to the image, and use a novel matched filter to detect the movers in this space. We can then image the moving targets using standard

SAR focusing techniques and geo-locate the movers using multi-channel (if available) along-track interferometry. We demonstrate and evaluate our algorithms using data collected from the LiMIT airborne radar system.

Index Terms

synthetic aperture radar, mover detection, gmti, mti

I. INTRODUCTION

Radar systems often use ground moving target indication (GMTI) to detect ground targets with speeds above a certain minimum detectable velocity (MDV) and synthetic aperture radar (SAR) for imaging large stationary scenes. These systems provide vital surveillance capability, particularly in the absence of optical/infrared, or during poor weather and cloud coverage.

This work describes a new algorithm for detecting and imaging moving targets in single or summed channel SAR imagery, building upon previous work in this area [1]–[3]. Detecting moving targets in SAR imagery (often called SAR-GMTI) has recently gained a lot of interest as a way to image and classify moving targets, and to mitigate GMTI performance gaps. Synthetic aperture radar (SAR) provides fine-resolution two dimensional mapping of stationary scenes and targets. Conventional SAR image formation algorithms assume a completely stationary scene: The significant distortion in a SAR image caused by even minor target motions prevents focused imaging of the movers and can obscure portions of the non-moving scene.

SAR-GMTI on the other hand aims to take advantage of the moving target blurring to detect the moving target. It is a difficult problem, but has a variety of important applications: since SAR-GMTI can detect movers at velocities significantly below normal GMTI's minimum detectable velocity, it could help improve conventional GMTI performance when both are run simultaneously, or replace GMTI when it is not available.

The apparent cross-range position of a moving target in a SAR image is a function of both the unknown true cross-range position and the velocity of the target. As such the SAR-GMTI problem can be broken into two parts: the detection of the target (apparent cross-range), and the determination of the target's velocity or of its true cross-range. The detection of a moving target in single channel SAR is usually done by taking advantage of the distortion in the SAR imagery caused by moving targets in order to separate the unfocussed moving targets from the focused stationary scene [1], [2]. The second problem is particularly difficult in single channel SAR as it can only be determined from the SAR data by looking for the absence of the target's energy or shadows caused by occlusion.

Many of the algorithms in the literature take advantage of multiple channel antennas which are able to determine the target's true in-range velocity to aid detection and provide geo-location. Some of the common multiple channel methods include space time adaptive processing (STAP) or displaced phase center antenna (DPCA) [4]–[7].

Page et al. combined constant acceleration target motion focusing with space-time adaptive processing (STAP), and included the refocusing parameters in the STAP steering vector. Due to inhomogenous clutter and limitations in spatial degrees of freedom, STAP performance alone in GOTCHA data was somewhat poor. To improve the detection and geo-location performance, they combine the STAP detection with change detection results for multiple-pass GOTCHA data [3]. For functionality in the absence of multiple-pass data, along-track interferometry (ATI) was also added to the STAP processing [8].

An interesting single channel detection method by J.R. Fienup was to perform autofocus in patches across the images [1], [2]. The locations of significantly improved focus after autofocus correction indicated the presence of movers. M. Jahangir on the other hand detected and geo-located moving targets by tracking the shadow of the target over multiple frames [9].

This work describes a new algorithm for detecting moving targets. We combine a number of the basic elements already mentioned in previous literature along with novel algorithm innovations, to generate a robust detection algorithm for single or multiple channel data. Our approach works on the data after SAR image formation and exploits the well focused SAR image to first enable removing most of the stationary scene. We apply a series of motion hypotheses to the image, and use a novel two-dimensional matched filter to detect the best focused hypothesis at each range bin. We then apply minimum entropy autofocus to image the target [10]. As available, multiple channel data can then be used to geo-locate the focused moving target. As the geo-location happens after the autofocus step, it will include coherent gain improvements provided by focusing the target.

We will demonstrate the algorithms and results using data from the Lincoln Multi-mission ISR Testbed (LiMIT) sensor. The LiMIT sensor is a high bandwidth, 0.5 meter antenna, mounted in the nose of a Boeing 707. The data presented here is at X-band and uses a single sum channel with 0.3 meter range and cross-range resolution. Additionally, 8 channel data is also available for all runs and is used in the final geo-location step. The LiMIT data contains high resolution SAR imagery of various locations near Sierra Vista, Arizona, including busy urban scenes as well as rural unpopulated scenes.

The range to scene center was between 18-30 km with around 20 degree grazing angles and 7-12

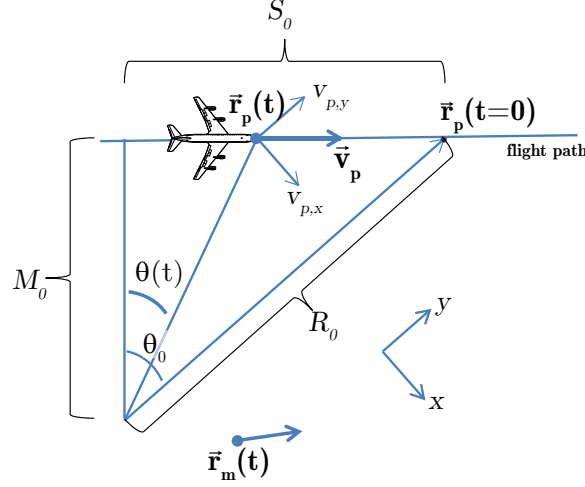


Fig. 1. Scene Geometry for a squinted straight line flight path.

seconds integration times. The SAR images were formed using polar format processing followed by map drift and minimum entropy autofocus. The final image sample spacing is 0.2 meters.

II. DERIVATION

Since a target's cross-range location is obtained from the Doppler induced by the motion of the sensor platform, a moving target in a conventionally focused SAR scene will display two distinct effects: First, the true cross-range position of a moving target is ambiguous with its in-range (i.e. line-of-sight) velocity. This will cause the mover's energy to be shifted in the image by an amount proportional to the target's in-range velocity. Second, the mover will be blurred in the image, both because the cross-range velocity will cause the mover to transition through multiple cross-range cells, and because any in-range velocity variation will cause the cross-range shift to vary.

In this section, the phase history for a moving target after SAR image formation is derived. The scene geometry is shown in figure 1. We will consider movers in spotlight SAR imagery after conventional image formation which includes polar formatting and autofocus techniques. The moving target's position is given by:

$$\vec{r}_m(t) = \begin{bmatrix} x_m(t) \\ y_m(t) \\ 0 \end{bmatrix}, \quad (1)$$

where $x_m(t)$, $y_m(t)$, $z_m(t)$ are the target's cross-range position, in-range position, and height respectively.

We assume that the sensor platform follows a linear trajectory, $\vec{\mathbf{r}}_p(t)$, at constant velocity, given by:

$$\vec{\mathbf{r}}_p(t) = \begin{bmatrix} v_{p,x}t \\ R_0 + v_{p,y}t \\ 0 \end{bmatrix}, \quad (2)$$

where $v_{p,x}$ and $v_{p,y}$ are the cross range and range velocities and R_0 is the ground range from scene center to flightpath midpoint. Time is aligned such that $t = 0$ is at the center of the synthetic aperture. The base coordinate x and y axes are aligned with the $t = 0$ cross-range and range axes. These coordinates are rotated from the along-track (platform flight path)/cross-track coordinate frame by the squint angle, θ_0 . For the purpose of simplicity, we remain in the slant plane by assuming that the height of the target and the sensor are zero.

Additionally, we will use some values from a coordinate system aligned with the platform flight path: M_0 and S_0 , which are the cross-track and along-track distances from the synthetic aperture center to the aim-point.

The complex phase history of the signal, in terms of wavelength λ and slow time t , of a moving target after matched filter and passband equalization processing can be expressed as:

$$P(t) = \exp\left(-j\frac{4\pi}{\lambda}\|\vec{\mathbf{r}}_p(t) - \vec{\mathbf{r}}_m(t)\|\right) \quad (3a)$$

$$\approx \exp\left(-j\frac{4\pi}{\lambda}\|\vec{\mathbf{r}}_p(t)\|\right) \exp\left(j\frac{4\pi}{\lambda}\frac{\vec{\mathbf{r}}_p(t) \cdot \vec{\mathbf{r}}_m(t)}{\|\vec{\mathbf{r}}_p(t)\|}\right), \quad (3b)$$

where (3b) is a commonly used far-field approximation [11] that comes directly from the first order Taylor expansion about $\mathbf{r}_m(t)$. The first term in (3b) is generally removed during the SAR image formation through motion compensation and autofocus. Substituting for $\vec{\mathbf{r}}_m(t)$ and $\vec{\mathbf{r}}_p(t)$, from equations 1 and 2, we get:

$$\tilde{P}(t) = \exp\left(j\frac{4\pi}{\lambda}\frac{\vec{\mathbf{r}}_p(t) \cdot \vec{\mathbf{r}}_m(t)}{\|\vec{\mathbf{r}}_p(t)\|}\right) \quad (4a)$$

$$= \exp\left(j\frac{4\pi}{\lambda}\frac{(v_{p,x}t)x_m(t) + (R_0 + v_{p,y}t)y_m(t)}{\|\vec{\mathbf{r}}_p(t)\|}\right). \quad (4b)$$

Next, we describe the conversion from range and Doppler to range and cross-range. This is often done using polar reformatting as described by Jakowatz et al. [12]. Polar format interpolates the phase-history of the collection in wavenumber space (chirp frequency by slow time) (λ, t) onto a rectangular grid. We define k_x and k_y be the spatial Fourier-transform wavenumber pairs of x and y respectively. The

transformation from $(\lambda, t) \rightarrow (k_x, k_y)$ can be geometrically shown to be:

$$k_x = \frac{4\pi}{\lambda} \sin[\theta(t) - \theta(0)] \quad (5a)$$

$$k_y = \frac{4\pi}{\lambda} \cos[\theta(t) - \theta(0)] \quad (5b)$$

Expanding the sine and cosines, and rewritting in terms of S_0 , M_0 , and R_0 , we get the following expression for k_x :

$$\begin{aligned} k_x &= \frac{4\pi}{\lambda} [\sin \theta(t) \cos \theta(0) - \cos \theta(t) \sin \theta(0)] \\ &= \frac{4\pi}{\lambda} \frac{M_0(S_0 + v_p t) - M_0 S_0}{R_0 ||\vec{\mathbf{r}}_p(t)||} \\ &= \frac{4\pi}{\lambda R_0} \frac{M_0 v_p t}{||\mathbf{r}_p(t)||}, \end{aligned} \quad (6)$$

A similar expansion for k_y gives:

$$k_y = \frac{4\pi}{\lambda R_0} \frac{R_0^2 + S_0 v_p t}{||\mathbf{r}_p(t)||}. \quad (7)$$

We combine (6) and (7) to solve for λ and t in terms of k_x and k_y :

$$\frac{4\pi}{\lambda} = \frac{||\mathbf{r}_p(t)||}{R_0} (k_y - \tan \theta_0 k_x) \quad (8a)$$

$$t = \frac{1}{\Omega_0} \frac{k_x}{(k_y - \tan \theta_0 k_x)} \quad (8b)$$

where $\tan \theta_0 = \frac{v_{p,y}}{v_{p,x}} = \frac{S_0}{M_0}$ is the tangent of the squint angle, and $\Omega_0 = \frac{v_{p,x}}{R_0}$ is the effective rotation rate of the scene at $t = 0$ due to airplane motion.

Plugging λ and t ref equation into the phase history (4b) gives:

$$\tilde{P}(t) = \exp\left(j[k_x \mathbf{x}(t) + k_y \mathbf{y}(t)]\right) \quad (9)$$

This result is consistent with the projection slice theorem [12], as well as the derivation by Scarborough et al. [3].

Since we will be applying the phase in k_x , after polar format, we desire to write the equations in terms of k_x only. We define $\tau = \frac{1}{\Omega_0} \frac{k_x}{k_y}$, and rewrite $\tilde{P}(t)$ in terms of τ :

$$\tilde{P}(\tau) = \exp\left(jk_y[\Omega_0\tau\mathbf{x}(\tau) + \mathbf{y}(\tau)]\right) \quad (10)$$

We can use equation 8b to find the relationship between t and τ :

$$\begin{aligned} t &= \frac{\tau}{1 - \tan\theta_0\Omega_0\tau} \\ t &= \tau(1 + \tan\theta_0\Omega_0\tau + (\tan\theta_0\Omega_0\tau)^2 + (\tan\theta_0\Omega_0\tau)^3 \dots) \\ &\approx \tau + \tan\theta_0\Omega_0\tau^2 \end{aligned} \quad (11)$$

Since Ω_0 is generally very small, often on the order $1/100$ or less, we have removed all Ω_0 terms of order 2 and greater.

We assume a polynomial form for the target's spacial motion in time, describing $x(t)$ and $y(t)$ to third order in t (constant jerk):

$$\begin{aligned} x(t) &= x_0 + v_x t + \frac{1}{2}a_x t^2 + \frac{1}{6}\gamma_x t^3 \\ y(t) &= y_0 + v_y t + \frac{1}{2}a_y t^2 + \frac{1}{6}\gamma_y t^3 \end{aligned} \quad (12)$$

where a_y , a_x are the target's range and cross-range acceleration, and γ is the jerk. We can then do a change of variables to get $x(\tau)$ and $y(\tau)$. We rewrite $x(t)$ in terms of τ as follows (a similar expression applies to $y(t)$):

$$\begin{aligned} x(\tau) &= x_0 + v_x(\tau + \tan\theta_0\Omega_0\tau^2) \\ &\quad + \frac{1}{2}a_x(\tau^2 + 2\tan\theta_0\Omega_0\tau^3) \\ &\quad + \frac{1}{6}\gamma_x(\tau^3 + 3\tan\theta_0\Omega_0\tau^4) \end{aligned} \quad (13)$$

Expanding the phase in equation 10 to third order, and substituting for x and y from equation 12 and 13, we get:

$$\begin{aligned}
\tilde{P}(\tau) \approx \exp \Big\{ & jk_y \left(y_0 + (\Omega_0 x_0 + v_y) \tau \right. \\
& + (\Omega_0 v_x + \frac{1}{2} a_y + \Omega_0 \tan \theta_0 v_y) \tau^2 \\
& + (\frac{1}{2} \Omega_0 a_x + \frac{1}{6} \gamma_y + \Omega_0 \tan \theta_0 a_y) \tau^3 \\
& \left. + \mathcal{O}(\tau^4) \right) \Big\}
\end{aligned} \tag{14}$$

The linear term in τ shows the ambiguity between a moving target's cross-range position and in-range velocity which is inherent to movers in SAR imagery—particularly with straight line flight path geometry as described here. The second order term will be the primary contributor to the target's cross-range blurring and will be dominated by a_y at low mover velocities. The exact form of this equation will vary depending on the flight path (straight vs curved), but both a_y and v_x will be significant contributors regardless of the flight path or amount of squint.

Some authors present methods for resolving cross-range ambiguity via a strict constant-velocity assumption [13]. The practical application of such methods will suffer due to navigational errors, but more, due to departures from the constant-velocity assumption. It is easy to show in simulations how a slight change in in-range velocity from early to late aperture will result in tens of meters of location error or more, depending on assumptions. We have chosen not to include a sensitivity analysis in the present paper.

III. MOVING TARGET DETECTION AND FOCUSING

Moving target processing can be split into three parts: detection, imaging, and geo-location. Here we will focus our discussion on detection (or summed) channel SAR data. We then briefly describe how we perform imaging as well as geo-location (geo-location only when multiple channel data is available).

Since we expect both the jerk (γ) and Ω_0 terms to be relatively low for the purpose of detecting the mover, we approximate the phase in equation 14 to second order in τ :

$$\begin{aligned}
\phi(\tau) \approx & k_y \left(y_0 + (\Omega_0 x_0 + v_y) \tau \right. \\
& \left. + (\Omega_0 v_x + \frac{1}{2} a_y + \Omega_0 \tan \theta_0 v_y) \tau^2 \right)
\end{aligned} \tag{15}$$

For the same reason that a constant velocity is a poor approximation, a constant acceleration is also often insufficient, but it usually will suffice for detection of the target. We will address the higher order terms after initial detections have been made on the target.

Additionally, to simplify the application of this phase we can make the approximation that $k_y = \frac{4\pi}{\lambda}$, which is k_y at $t = 0$. Additionally, we can approximate $\lambda = \lambda_0$, where λ_0 corresponds to the center frequency of the radar. This approximation is equivalent to ignoring the range walk, which may or may not be desirable based on what operation we are performing and on what the sensor parameters are.

The second order term gives us the characteristic blurring phase term we will use to detect the moving target, similar to [3]:

$$P(\tau) = \exp\left[-j\frac{4\pi}{\lambda}\left(\frac{1}{2}a_e\tau^2\right)\right] \quad (16)$$

$$a_e = 2\Omega_0 v_x + a_y + 2\Omega_0 \tan \theta_0 v_y \quad (17)$$

We will utilize this characteristic blurring function to detect the moving targets in a SAR image after being polar formatted and autofocused. The main steps of the algorithm, each of which we will describe in detail, are:

- Background suppression: we first estimate and remove the stationary background from the focused SAR image
- Motion compensation: we correct the SAR image formation for a set of possible moving target motion hypotheses
- Mover detection: we apply a matched filter in the motion hypothesis domain to detect the moving targets and the most likely motion hypothesis
- Target segmentation and focusing: we segment out the target in motion, range, and Doppler, and apply SAR autofocus algorithms to extract the full target motion compensation
- Target geo-location: If multiple channel data is available the target can be geo-located using ATI processing

The second to last steps are iterated per range-bin as each mover is detected and removed from the SAR image. Additionally, when processing capacity is limited, it can be useful to apply a pre-filter (usually a local sum over cross-range) after the background removal to find horizontal streaks in the image and to detect the most likely ranges to contain moving targets. It is also usually not necessary to do detection processing on every single range bin (evaluating every other or even every five range bins gave good results for the data set we used).

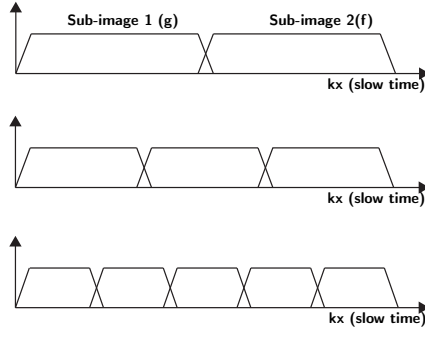


Fig. 2. Multi-resolution background subtraction

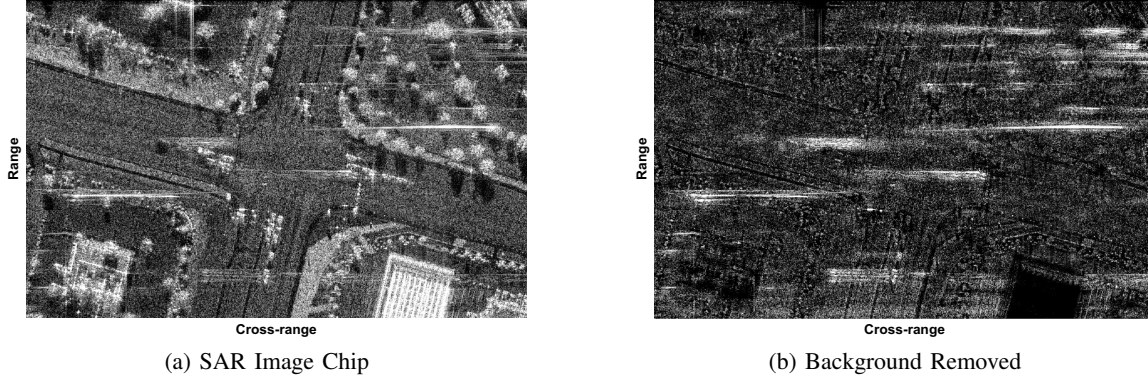


Fig. 3. Left: a chip from the original SAR image near a busy intersection. Many moving and accelerating targets can be seen as faint horizontal streaks in the image. Right: the same chip after clutter removal. The streaks due to the moving targets are much stronger and easier to discern in this image.

A. Background Suppression

An important first step in mover detection is stationary target suppression. If we do not first suppress the stationary scene, then after we apply the motion hypotheses to detect the movers, stationary objects will smear out, obscuring or reducing SINR on the focused moving targets. We propose a non-coherent subtraction of short time subapertures to remove the stationary scene. Note that k_x is equivalent to τ , our slow-time indicator, if k_y is fixed. We use multiple time-subaperture resolutions in order to alleviate subimage subtraction discontinuities at the k_x boundary between images.

The algorithm works as follows, with each resolution dividing the original SAR image into N sub-images (we used $N = 2, 3, 5$):

- 1) Fourier transform the cross-range dimension of the image to k_x
- 2) Remove time-domain amplitude window
- 3) Divide the time domain into N equal sections
- 4) Inverse Fourier each section back to the cross-range domain
- 5) Calculate CFAR difference statistic for all possible sub-image combinations and average the results

- 6) Upsample the statistic back to full image resolution
- 7) Repeat the previous steps for all N resolutions, then average over all resolutions (N) to get an initial mask
- 8) Apply the mask to the original complex SAR image
- 9) Apply additional thresholding and blanking
- 10) Reapply the time-domain amplitude window in the k_x domain to get the final background subtracted complex image

The multi-resolution sub-image setup is shown in figure 2 for $N=2,3$ and 5. The selection of prime numbers for N ensures that the k_x sub-image boundaries never line up at the same position across all resolutions. After we have divided the image into N low resolution sub-images, a constant false alarm rate (CFAR) statistic provides a useful normalized measure for the sub-image subtraction. We found the following CFAR statistic to be effective:

$$\gamma = \frac{\sum_i ||f_i| - |g_i||}{\sum_i ||f_i| + |g_i||} \quad (18)$$

where the sum is done over a small 5×5 window in range and cross range, and f_i is the first time-subimage and g_i is the second. The output is a lower resolution, magnitude only, difference image. We apply this statistic to all possible image pair combinations at a given resolution, average the result for each resolution, and then upsample back to the original image resolution. Once we have obtained upsampled results for all resolutions, we average these into a continuous (magnitude only) mask.

We then apply this mask directly to the complex SAR image, by multiplying the original SAR data by the smoothed magnitude of the SAR image divided by the smoothed magnitude of the difference mask:

$$I_b = \frac{\tilde{\gamma}}{|\tilde{I}_0|} I_0 \quad (19)$$

where I_0 is the complex focused SAR image, $|\tilde{I}_0|$ is the smoothed magnitude SAR image, and $\tilde{\gamma}$ is the smoothed difference mask. This retains both all of the complex data as well as some of the local intensity variation from the original SAR image. Both images were smoothed with an identical 13×17 flat-top smoothing filter.

In order to mitigate bright stationary points and to handle speckle noise, we apply a set of thresholds to the mask based on both the brightness of the points in the original image and the value of the difference

statistic. The specifics will likely change for each system but here we applied the following thresholding: All points in the final background subtracted image are zeroed out unless they are above a difference level statistic threshold or below an amplitude threshold (low enough to allow clutter in). This allowed us to detect moving targets that had blurs with energy below the speckle clutter level (eg. grass or roads) in the image. Additionally, it is useful to zero out very bright point scatterers.

Figure 3a shows the initial focused SAR image of an intersection of an urban area near the Sierra Vista Walmart, with numerous non-instrumented moving vehicles and people. Figure 3b shows the scene after background removal. We can see that most of the stationary clutter has been significantly reduced in power, while the moving target blurs are accentuated.

Unlike multiple channel based clutter removal, this clutter removal depends only on the target in-range acceleration and cross-range velocity, not on its range-rate. As such any accelerating target will be detectable regardless of how low its average speed is.

One possible problem with the procedure described here is that since the time domain amplitude profile of the moving target is changed by this processing, it can cause artifacts in the target focusing. Although it is possible to instead use the background removal mask in binary fashion to try to avoid this problem, we found better detection rates and focusing performance using the direct application of the mask onto the complex data as described here.

B. Motion Compensation

In order to focus and then detect the moving targets, we apply a set of motion hypotheses to the SAR image. Approximating $k_y = k_{y0}$, where k_{y0} corresponds to λ_0 (at $k_x = 0$), we can describe our motion models application as a Fourier transform over k_x :

$$s'(x, a_e, r_i) = \int s(k_x, r_i) \exp \left[-j \left(\frac{\lambda_0}{8\pi\Omega_0^2} a_e k_x^2 + x k_x \right) \right] dk_x \quad (20)$$

where $s(k_x, r_i)$ is the fourier transform of our background removed SAR image at range r_i .

Each motion hypothesis is applied as a quadratic phase in the k_x domain, to a single range bin. We can plot the results as a function of acceleration hypothesis and cross-range. We can see the resulting output on simulated data in Fig. 4. The X or hourglass shape we see in this plot is characteristic of focusing moving targets: The energy focuses up to a point as the motion hypothesis approaches the correct value and then defocuses as too much compensation is applied.

It is worth mentioning that although the acceleration induced range walk does have a non-negligible effect on many of the movers, we have found that the mover's energy stays in the same range bin for long enough for the mover target detection to work without any range walk correction. Most of the detection processing we will show works on a single-range at a time and thus does not include a range walk correction. At long integration times, a range-walk correction is likely to become necessary and the processing can easily be adjusted to handle range-walk by including multiple range lines and applying the quadratic phase correction in (λ, t) .

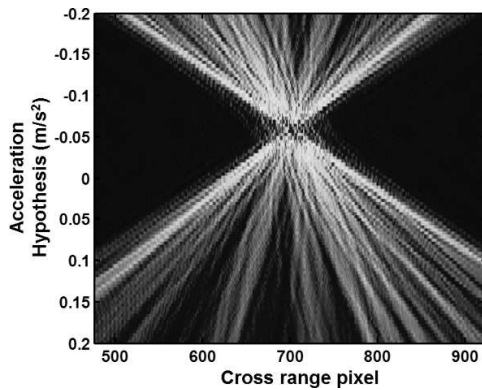


Fig. 4. The acceleration vs. cross-range plot of a simulated (with some random time-domain amplitude fluctuations) point scatterer with a non-zero acceleration. The point scatterer focuses up at the correct input acceleration (-0.06 m/s).

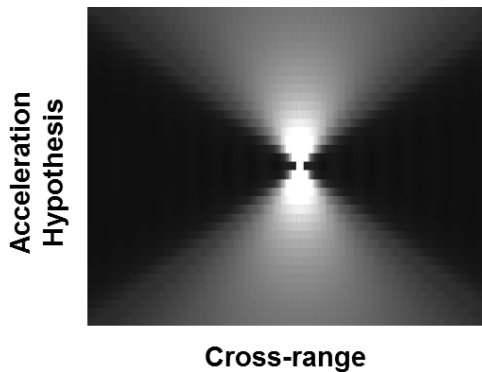


Fig. 5. The acceleration vs. cross-range plot of an ideal point scatterer, which is used for the 2-D matched filter detector.

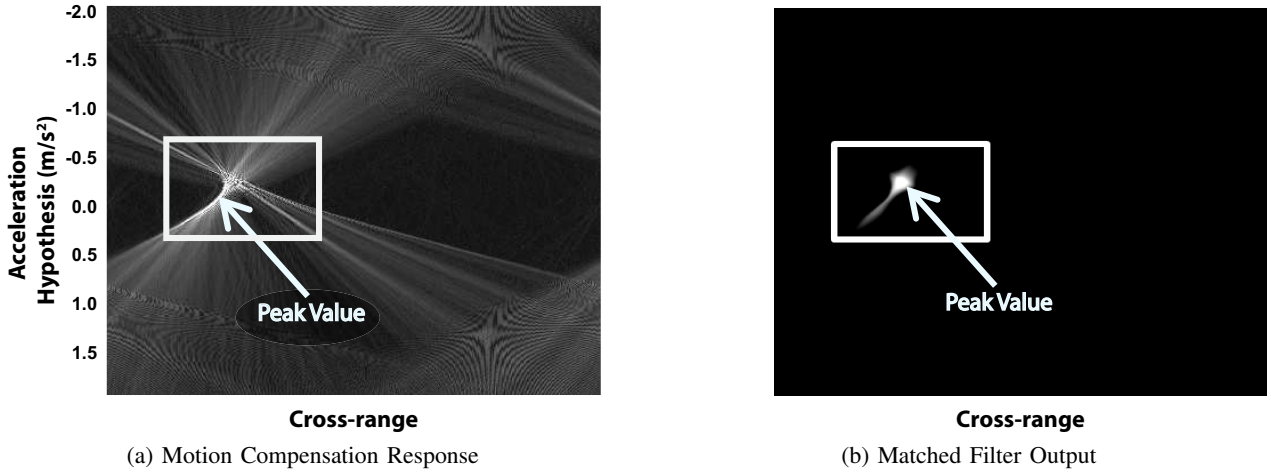


Fig. 6. Left: The response across cross-range of a single range bin of a mover to a variety of motion hypotheses. Right: The resulting score plot convolving the motion response with the 2-D matched filter. While for the original response function (left), the brightest point gives an poor motion estimate, the response to the 2-D matched filter provides a much better estimate.

C. Two Dimensional Matched Filter

In figure, 6a, we have plotted the motion vs cross-range plot for a mover taken from the LiMIT data. Although the energy focuses up, it does so imperfectly. This is due to higher order phase terms that are not modeled by our second order phase correction. The best focused energy (correct quadratic hypothesis) is both broadened, and contains significant interference fringes. These distortions create a situation where the brightest peak in the motion vs cross-range plot is significantly offset from the desired result. This is a common occurrence for real moving targets, which often experience non-constant accelerations.

Since it is computationally prohibitive to try to apply higher order motion hypothesis, we propose the following solution: In order to detect the closest second order motion hypothesis in the presence of noise and the higher order terms, we convolve the motion and cross-range image of each selected range bin with the impulse response of an ideal point scatterer in acceleration and cross-range. This two-dimensional matched filter aims to provide an accurate estimate of the most likely motion hypothesis for a given point scatter based on the X or hourglass shape of the entire hypothesis vs cross-range plot.

We describe the impulse response of an ideal point scatterer in cross-range:

$$h(a_e, x) = \int W(\tau) \exp\left(-j\frac{4\pi}{\lambda}\left(\frac{1}{2}a_e\tau^2 + \Omega x\tau\right)\right) d\tau \quad (21)$$

where τ is evaluated at $k_y = \frac{4\pi}{\lambda_0}$ and $W(\tau)$ should be set to be identical to the time-domain windowing applied to the SAR image. The resulting filter kernel is shown in figure 5. The matched filtering then proceeds as follows:

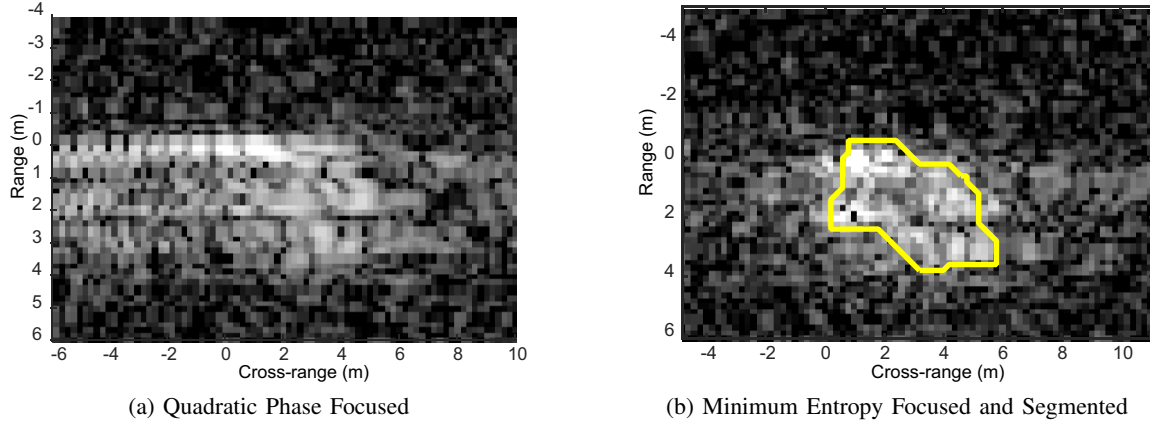


Fig. 7. Left: The partially focused moving target chip after motion hypothesis based focusing. Right: The same chip after minimum entropy autofocus. The yellow outline indicates the automatic target segmentation.

$$\text{score}(x, a_e) = \hat{h}(x, a_e) * \hat{s}(x, a_e) \quad (22)$$

Where we have subtracted the mean over both x and a_e , $\langle \rangle$, from the filter and signal equations, and normalized the matched filter:

$$\hat{h}(x, a_e) = \frac{|h(x, a_e) - \langle h(x, a_e) \rangle|}{\|h(x, a_e) - \langle h(x, a_e) \rangle\|^2} \quad (23)$$

$$\hat{s}(x, a_e) = |s(x, a_e) - \langle s(x, a_e) \rangle| \quad (24)$$

This provides a final score that is both dependent upon the power of the signal and the shape similarity.

We can see the resulting score in figure 6b. It clearly accentuates the location which is closer to the center of the hourglass shape, while de-emphasizing the bright streak to the lower left of the shape. This provides a accurate estimate of the true second order term in the motion of the target. Note that although we have described the hypothesis term in units of acceleration, we cannot determine how much of the term actually represents cross-range velocity versus in-range acceleration.

D. Target Segmentation and Imaging

Once a target has been detected, it must be focused, and then the target's energy can be extracted from clutter (segmentation). We first re-apply the estimated quadratic phase focusing function (determined above), and this time include the full range-walk correction (see (16)). We select a target chip with enough

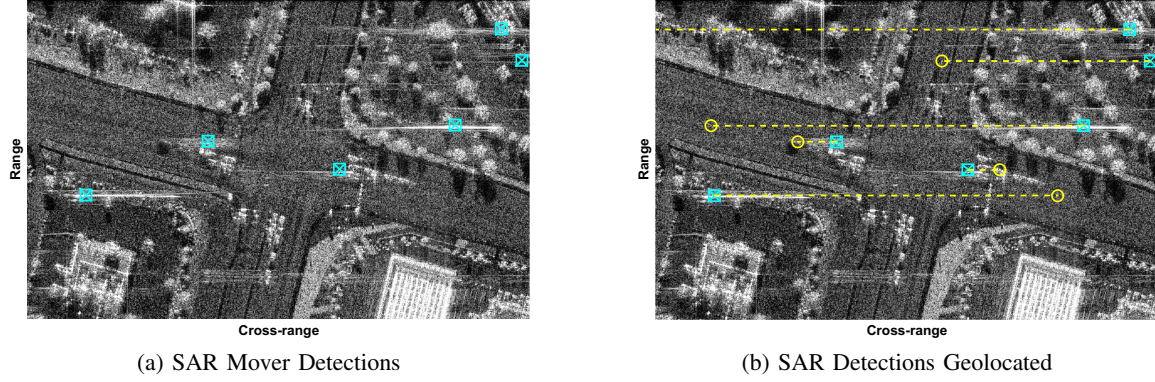


Fig. 8. Left: The top 6 moving target detections for the SAR image chip of this intersection, indicated by blue squares. Right: The detections along with the estimated target geolocations, indicated by yellow circles.

range bins near the target to entirely encapsulate any target of interest and a generous box in cross-range to fully include the target's blurred energy. We then apply minimum entropy autofocus [10] to find a general motion solution that will fully focus the extracted target chip.

Once the target is focused we use the following segmentation algorithm to precisely segment the target energy. To do so, we take advantage of the previously defined 2-D matched filter.

We reuse equations 22 and 23 but change equation 24, so that it is now normalized as well:

$$\hat{s}'(x, a_e) = \frac{|s(x, a_e) - \langle s(x, a_e) \rangle|}{||s(x, a_e) - \langle s(x, a_e) \rangle||^2} \quad (25)$$

This normalization removes the power dependence from the equation, providing a result that is only shape dependent:

$$score_{mf}(x, r) = (\hat{h}_r(x, a_e) * \hat{s}'_r(x, a_e))^2|_{a_e=0} \quad (26)$$

Additionally, we now use the power as a separate feature for segmentation:

$$score_{mag}(x, r) = |s(x, r)|^2; \quad (27)$$

This feature separation allows us to perform a two-class (target and non-target) Gaussian classifier in two dimensions ($score_{mag}$ and $score_{mf}$). We used a limited quantity of manually labeled data to train the classifier, as well as performing some adaptive tuning on a per chip basis. Once peaks were classified, we used morphological image filtering on the classified peaks to define a section of the image, and outline the target.

Figure 7a shows an image chip after the initial quadratic phase focusing. The target in this image is more focused than in the original image, and most of the range walk has been removed, but we can still see significant blurring in the target's energy. Figure 7b shows the target after minimum entropy autofocusing. The segmentation described here is visualized by the yellow line around the target, indicating the precisely selected target outline.

After focusing, the target energy can be extracted from the image. A separate target chip is made (which could be placed in the image at the correct location, if geolocation can be performed) and the blurred energy of the target is subtracted from the image so that future iterations of the algorithm will not detect the target. Finally, after extracting each target, we iterate the detection algorithms to find additional targets.

E. Geo-location

Although most of the work is done in single or the summed channel, it is also useful to consider possible places where using multiple channels can be useful. In this work, we use multiple channels for geo-location on the LiMIT data. Shadows can also be used to assist in geolocation [14], but since that only works for very slow movers, and since our SINR was too low to get really consistent shadows, we do not show any results with shadows here.

In order to geo-locate the detected movers, we first polar format and autofocus each channel separately, and then apply an overall phase alignment between the channels. Each channel is polar formatted onto an identical grid in k_x and k_y such that the channels are shifted to be aligned with each other in space. The phase alignment then consists of a single phase offset for each channel, which can be easily determined from the data.

The multiple channel geolocation is done after the detection, segmentation, and full autofocus have been performed on the sum channel data, and the results applied to each individual channel. We use along-track interferometric processing [8]. By measuring the phase ramp as a function of channel, across the detected and segmented target, we can determine the appropriate geo-location of the target. Since this is done after focusing, we will get the full coherent gain from the focused target energy. There is an additional phase error across the antenna aperture resulting from target movement in cross-range but since the antenna aperture is small and the targets are generally moving slowly, it will be a relatively small effect and we ignore it here.

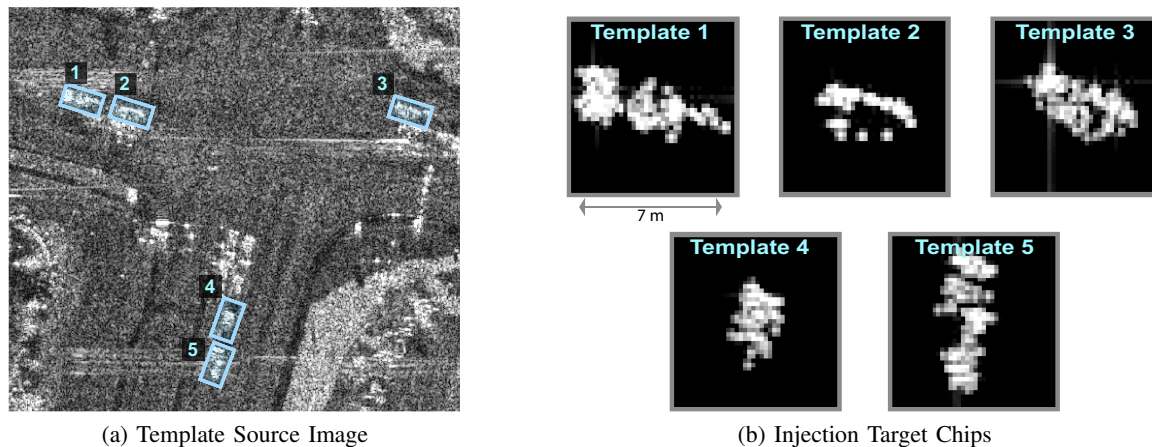


Fig. 9. Injections use templates extracted from real targets, stopped at the intersection. Figure 9a shows the original SAR image of the intersection, and figure 9b shows the extracted target templates.

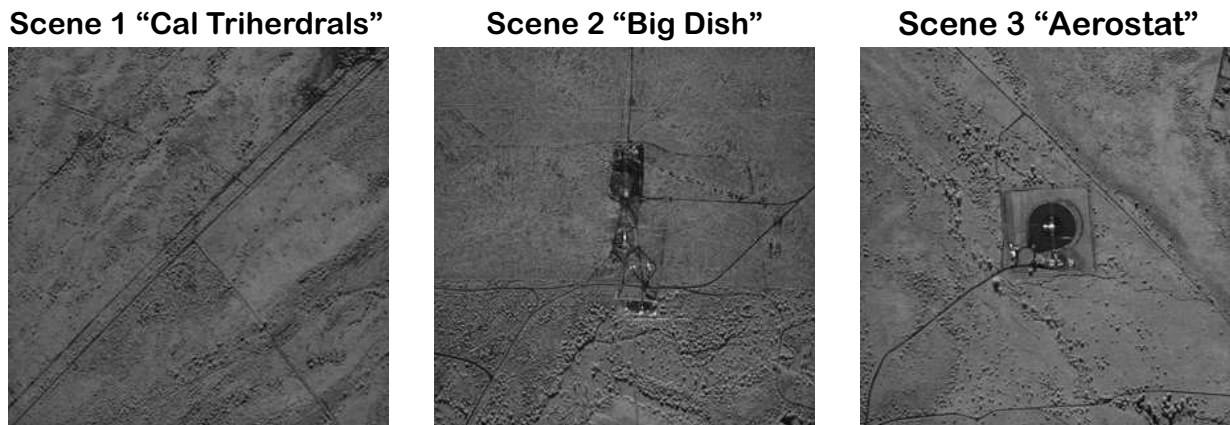


Fig. 10. SAR images of the three rural scenes used for the injection analysis.

Figure 8a shows the strongest 6 detections in our SAR image chip. We can see these clearly lie on moving target blurs. The yellow circles in Figure 8b show the estimated geo-locations of the detected targets. In each case, the geolocations lie on the road very close to where we would predict the actual movers to be located. In fact, we can see the shadow of the moving target on the left side of the intersection, indicating its true geolocation, and directly above that, the multiple channel estimated geolocation.

IV. RESULTS AND ANALYSIS

The LiMIT data collection did not include truth for any moving targets in the scene. Therefore, we propose a realistic target injection method. First, we select stationary vehicles from the focused SAR image of the Urban scene by hand. We manually precisely outline the energy of the target we wish to use. We then apply a method similar to the CLEAN [15], [16] algorithm, and iteratively select point scatterers from the target area (usually about 20-30 scatterers are used).

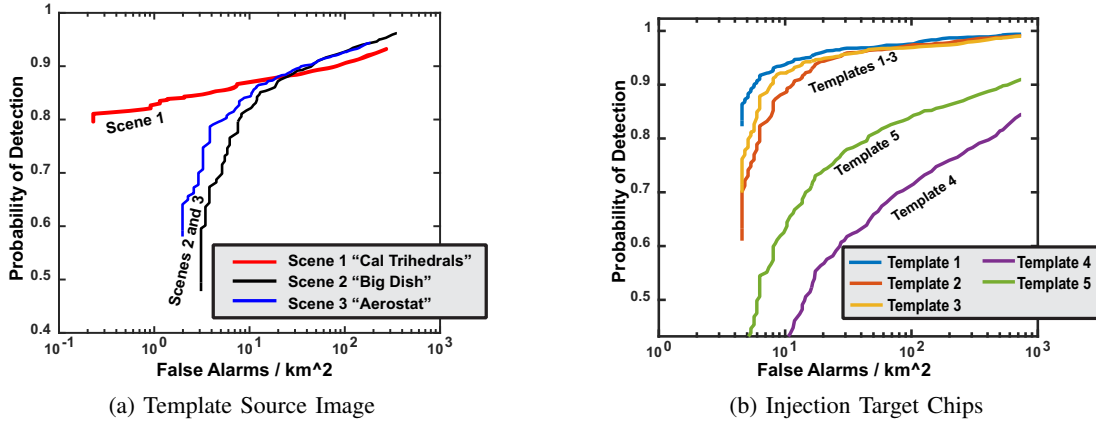


Fig. 11. ROC curves (detection vs false alarm rate) for the injected targets broken down by scene number (left) and template number (right).

These point scatterers are then injected into the LiMIT SAR imagery using their ideal point response with motion based blurring. In order to create a larger amount of target variety, we run a monte-carlo experiment with random variation applied to the parameters of the injected targets, including target motion, target power, Doppler and range offsets, and vehicle chip number.

Motion based defocusing is applied to the chips according to equation 10 in section II. In this study, the motion is assumed to be linear (no turning) motion and includes 3rd and higher order terms. Precisely, the target's motion consists of 3 steps: A constant initial acceleration, a linearly changing acceleration, and then a final constant acceleration. The starting acceleration, ending acceleration, and the amount of time spent in each step is all selected randomly for each sample (the max acceleration is varied between $\pm 0.3 \text{ m/s}^2$).

Figure 9a shows the source image containing the targets and figure 9b shows the extracted target templates. The five targets include small and large vehicles (4.5 to 7.5 meters), at two different aspect angles. At each injection, a target template is randomly selected from the available set. The target power is also varied so that the targets span around 20 to 40 dB peak SINR over all of the chips for every scene (measured using the mean of the top peaks in the target chip and the median of the SAR image).

For memory reduction purposes the 6500×6500 pixel SAR image is divided into 4 quadrants, and 29 targets are injected into each quadrant. The targets injected along the central cross range in each quadrant and then are shifted by random amounts in range and cross-range.

A total of seven images are used which include three rural scenes using two to three different aspect angles for each. The three scenes are shown in figure 10. Although each scene has some man-made features, including small roads, buildings, radar dishes, etc, they mostly consist of natural terrain—trees,

bushes, grass, and dirt. For the most part, no moving target activity is readily visible in any image. Each SAR image is used many times, which for the entire study results in a total of 7946 injected targets.

To generate the ROC curve, we used a combination of two thresholds: The peak scatterer energy in the detected target, and a metric representing the total amount of focusing performed on the target chip [1]. The second metric was very effective at reducing the number of false alarms. In order to independently evaluate the false alarm rate, we perform our false alarm analysis on the scene without any injected targets.

The results are shown in figure 11. In figure 11a, we plot each scene as a separate curve in the chart. We can see that the detection rate peaks at around 90 – 95% with 10-100 false alarms per square km. Scene 1 gives the lowest false alarm rates at reasonable detection rates. Many of the false alarms in scenes 2-3 are caused by man-made objects, including flashing power lines (which look very similar to moving targets), and radar dishes. Additionally, some of the reported false alarms are likely to be true moving target detections as we have no way of ensuring that the scenes were completely free of moving targets.

In figure 11b, we compare the results for different target types. The targets that are smaller, particularly in cross-range extent and peak dB, are significantly harder to detect. Additionally, because the motion is randomly varied, some of the missed detections come from nearly stationary targets.

V. SUMMARY

We presented here an algorithm to solve the problem of detecting movers in a single channel SAR system. The algorithms were demonstrated to be effective at detecting and focusing movers in LiMIT radar data. In addition, we used multiple channels to geo-locate the targets after they were detected. Although it is useful to demonstrate the detection of the targets in single channel, multiple channels could be used for detection as well and combining multiple channel information with the non-coherent time-based background suppression is an interesting topic for future study.

Along with describing our algorithms, we also attempted to quantify our single channel detection results using a monte-carlo simulation with realistic injected targets, and demonstrate good detection and false alarm rates. We can achieve good detection rates, even well below MDV. Compared to GMTI though, we expect that we would have significantly lower area coverage rate due to the longer integration times required for the high resolution in SAR imagery. We would therefore expect a SAR based GMTI system to work particularly well for cases where we were interested in detecting and tracking a few targets of interest—especially if those targets are likely to spend any time at below MDV speeds.

REFERENCES

- [1] J. Fienup, "Detecting moving targets in sar imagery by focusing," *Aerospace and Electronic Systems, IEEE Transactions on*, vol. 37, no. 3, pp. 794–809, July 2001.
- [2] S. Barbarossa and A. Scaglione, "Autofocusing of sar images based on the product high-order ambiguity function," *Radar, Sonar and Navigation, IEE Proceedings -*, vol. 145, no. 5, pp. 269–273, Oct 1998.
- [3] D. Page, G. Owirka, H. Nichols, S. Scarborough, M. Minardi, and L. Gorham, "Detection and tracking of moving vehicles with gotcha radar systems," *Aerospace and Electronic Systems Magazine, IEEE*, vol. 29, no. 1, pp. 50–60, Jan 2014.
- [4] Z. Suo, Z. Li, and Z. Bao, "Multi-channel sar-gmti method robust to coregistration error of sar images," *Aerospace and Electronic Systems, IEEE Transactions on*, vol. 46, no. 4, pp. 2035–2043, Oct 2010.
- [5] M. Soumekh, "Moving target detection and imaging using an x band along-track monopulse sar," *Aerospace and Electronic Systems, IEEE Transactions on*, vol. 38, no. 1, pp. 315–333, Jan 2002.
- [6] M. I. Pettersson, "Detection of moving targets in wideband sar," *IEEE Transactions on Aerospace and Electronic Systems*, vol. 40, no. 3, pp. 780–796, July 2004.
- [7] J. Sharma, C. Gierull, and M. Collins, "The influence of target acceleration on velocity estimation in dual-channel sar-gmti," *Geoscience and Remote Sensing, IEEE Transactions on*, vol. 44, no. 1, pp. 134–147, Jan 2006.
- [8] V. Murthy, F. Uysal, and S. Scarborough, "Target geolocation in gotcha data using cross-channel interferometry," in *2014 IEEE Radar Conference*, May 2014, pp. 0017–0021.
- [9] M. Jahangir, D. Blacknell, C. Moate, and R. D. Hill, "Extracting information from shadows in sar imagery," in *Machine Vision, 2007. ICMV 2007. International Conference on*, Dec 2007, pp. 107–112.
- [10] T. Kragh, "Monotonic iterative algorithm for minimum-entropy autofocus," in *Proceedings of the MIT Lincoln Laboratory, Adaptive Sensor Array Processing Workshop*, 2006.
- [11] W. C. Carrara, R. Goodman, R. Majewski, and B. Williams, *Spotlight Synthetic Aperture Radar: Signal Processing Algorithms*. Artech House Publishers, 1995.
- [12] C. V. Jakowatz, D. E. Wahl, P. H. Eichel, D. C. Ghiglia, and P. A. Thompson, *Spotlight-Mode Synthetic Aperture Radar: A Signal Processing Approach*. Norwell, MA: Kluwer Academic Publishers, 1996.
- [13] J. Yang, Y. Zhang, and X. Kang, "A doppler ambiguity tolerated algorithm for airborne sar ground moving target imaging and motion parameters estimation," *IEEE Geoscience and Remote Sensing Letters*, vol. 12, no. 12, pp. 2398–2402, Dec 2015.
- [14] T. Sparr, R. Hansen, H. Callow, and J. Groen, "Enhancing target shadows in sar images," *Electronics Letters*, vol. 43, no. 5, pp. 69–70, March 2007.
- [15] J. Tsao and B. D. Steinberg, "Reduction of sidelobe and speckle artifacts in microwave imaging: the clean technique," *IEEE Transactions on Antennas and Propagation*, vol. 36, no. 4, pp. 543–556, Apr 1988.
- [16] Y. Sun and P. Lin, "An improved method of isar image processing," in *Circuits and Systems, 1992., Proceedings of the 35th Midwest Symposium on*, Aug 1992, pp. 983–986 vol.2.